T.3: Measurement of longitudinal and transverse beam parameters of Indus-2 with synchrotron radiation based diagnostics

Akash Deep and T. A. Puntambekar
Beam Diagnostics and Coolant Systems Division
Email: akash-deep@rrcat.gov.in

Abstract

Indus-2 is an indigenously built third generation Synchrotron Radiation Source (SRS) with 2.5 GeV energy and 200 mA beam current, operating at RRCAT, Indore. It has a provision of 21 beamlines based on bending magnet and additional 5 beamlines based on insertion devices. Precise measurement of the electron beam parameters is very important to control the beam through narrow vacuum chambers of the accelerator. Various types of diagnostic devices are installed in the ring. However, there are certain beam parameters such as beam size, beam emittance, bunch length, bunch filling pattern etc. which can be better measured by optical methods using synchrotron radiation (SR) beamlines. Two diagnostic beamlines, viz. visible diagnostic beamline (V-DBL) and x-ray diagnostic beamline (X-DBL) have been designed, developed and commissioned at dipole magnet DP-10 in Indus-2. In the x-ray diagnostic beamline (BL-24), pinhole array system is used for measurement of size, emittance, position and divergence of the electron beam. And, the visible diagnostic beamline (BL-23) uses visible light of the SR spectrum for longitudinal measurements such as bunch length, bunch separation, bunch filling pattern etc. Both of these beamlines are used regularly for online monitoring of the above listed beam parameters, and also for the dedicated beam physics experiments. A brief introduction of the SR based measurement schemes used at diagnostic beamlines BL-23 and BL-24 in Indus-2 is given, and measurement of the longitudinal and transverse beam parameters of electron beam is explained in this article. Results of the measurement of beam position, beam dispersion, and ring impedance are also discussed. Design scheme of synchrotron radiation interferometer for visible diagnostic beamline in Indus-2 is also covered. The design has potential for measurement of small beam sizes.

1. Introduction

The motion of electrons in a SRS is guided by an external magnetic field lattice created by periodic arrangement of dipole, quadrupole, sextupole and steering magnets. The electrons confined within the bunch execute betatron oscillations about the closed orbit in transverse planes and synchrotron oscillations about the synchronous phase in longitudinal plane. The electrons within a bunch are continuously scattered due to elastic and inelastic scattering within the same bunch i.e. Touschek effect, and also with the residual gas atoms present in the vacuum chamber. The quality of the stored beam also depends upon the electromagnetic interactions of the beam with its surroundings, such as radio frequency (RF) cavities, narrow gap insertion devices and various discontinuities along the vacuum chamber. These interactions can also lead to deterioration of the quality of stored beam or may make the beam unstable [1]. Further, the demand to get high brightness SR has led to the production of beams with low emittance. However, particles confined in the smaller phase space are more prone to instability or beam loss. Therefore, in modern SRS facilities producing smaller and smaller beam (for higher SR brightness) puts more and more stringent requirements on the performance of the beam diagnostics [2].

Although various types of diagnostic devices are installed in the ring, but there are certain beam parameters which can be better measured and analysed by optical methods such as synchrotron radiation [3, 4], optical transition radiation [5], and diffraction radiation [6]. These are based on the principle that the emitted radiation has inherited information of the particle distribution from the electron beam. SR is a very versatile, efficient and non-destructive tool for characterization of the relativistic charged particle beam.

Two diagnostic beamlines, viz. visible diagnostic beamline and x-ray diagnostic beamline have been designed, developed and commissioned at dipole magnet DP-10 in Indus-2 [7, 8]. Former is mostly used for longitudinal measurements whereas the latter is used for transverse measurements. A brief introduction of the measurement schemes used at diagnostic beamlines BL-23 and BL-24 in Indus-2, and results of the measurement are discussed in the following subsections.
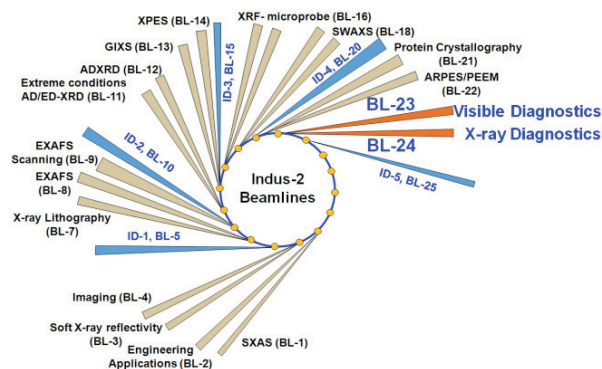
Fig. T.3.1: Schematic layout of the Indus-2 beamlines. Diagnostic beamlines BL-23 and BL-24 are also shown along with other user beamlines.

2. X-ray diagnostics

Advanced SRS facilities are being designed to have low emittance. The corresponding beam size reduces to few tens of microns in the bending magnet sections. Precise measurement of such a small transverse beam size is a challenging task. Measurement of transverse beam size by visible SR imaging is limited by diffraction. X-ray imaging optics using Fresnel zone plates (FZP) [9], compound refractive lenses (CRL) [10], Kirkpatrick and Baez optics [11], and pinhole camera [12], are commonly used for the transverse measurements. Each method has its own advantages and limitations. FZP and CRL have better resolution, but to avoid large chromatic aberrations both require monochromatic light. Resultantly, the photon flux arriving at the detector becomes very low and difficult to measure at low beam currents. An x-ray pinhole camera is widely used because of its simple setup, moderate resolution and high practical reliability.

2.1 X-ray diagnostic beamline BL-24

It is based on pinhole array imaging [7]. Tungsten pinhole array with 17(H) X 21(V) pinholes of 20 µm diameter each is placed at 8 m from the source point, and its imaging is carried out on a P-43 phosphor screen with a magnification factor of 1.2. The phosphor screen converts the x-rays into visible light for measurement with a CCD camera. The beamline is designed to capture image of more than five fully resolved pinholes on the phosphor screen. The schematic of the X-DBL is shown in Figure T.3.2.

The front-end (FE) of a beamline connects the beamline with the storage ring [13]. It starts right from the source port and extends upto Beryllium window outside the shielding tunnel. FE acts as an interface between the storage ring and the optical components of the beamline. It consists of a set of ultra high vacuum components with associated control and interlocks. Its main functions are vacuum protection of the ring, defining the angular acceptance of beamline, absorption of heat and user safety. Standard FE components used in X-DBL are collimator, water-cooled shutter (WCS), gate valves, fast shutter, safety shutter (SS), fixed mask and delay line chamber.
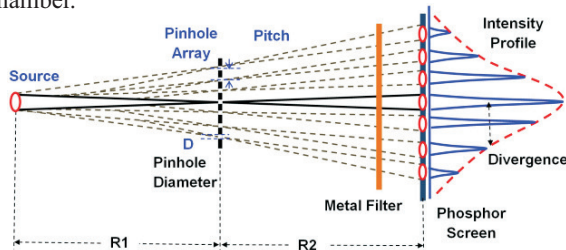
Fig. T.3.2: Schematic of the pinhole array based beam diagnostics employed in X-DBL.

An additional staggered pair blade monitor (SPM) is also installed inside the pinhole array chamber. It provides the vertical position of the photon beam at the location of pinhole array.

2.2 Pinhole array

The final image formed by the pinhole camera is the convolution of the source profile, and the contributions of the point spread functions (PSFs) of pinhole, phosphor screen, imaging optics and CCD camera. Consequently, the total convolved PSF of the beamline determines the smallest measurable image size at the beamline. The spatial resolution of the pinhole camera (σ_{Pin}) is mainly limited by diffraction and geometrical effects [14] as

$$\sigma_{Pin.} = \sqrt{(\frac{\sqrt{12}}{4\pi}\frac{\lambda R2}{D})^2 + \left(\frac{D(R2 + R1)}{\sqrt{12}\ R1}\right)^2} \qquad (1)$$

where λ is the wavelength, D is the pinhole diameter, $R1$ is the source to pinhole distance, and $R2$ is the pinhole to phosphor screen distance. These effects are optimized to get optimum diameter for the best possible resolution.

Pinholes are exposed to white SR beam having photons of all energies coming from the source. Metal filters assembly is used for energy selection and it acts as a high energy pass system. Results of variation in width of the pinhole spread function with pinhole diameter for different photon energies are plotted in Figure T.3.3. Pinhole diameter of ~20 µm has the lowest spread function width for photons in the energy range of 8-19 keV.
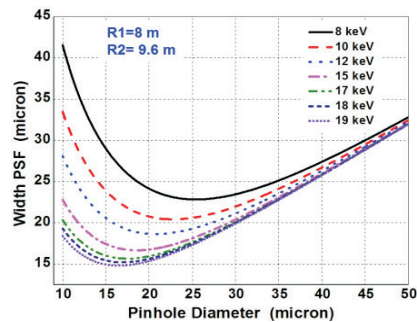
Fig. T.3.3: Variation in width of pinhole spread function with pinhole diameter at different photon energies.

The pinhole size is also optimized to get sufficient photon flux for imaging at the phosphor screen. SR code SPECTRA [15] is mostly used for calculations of flux and power density. In X-DBL, pinholes of ~20 µm diameter are best optimized for the lowest spread function width and detectable transmission of photon flux for imaging at the phosphor screen. 250 µm thick Tungsten pinhole array is sandwiched between the two

copper plates of 5 mm thickness, and proper water cooling is provided at its base to restrict the thermal deformations. The pinhole system provides good spatial resolution of ~ 20 µm for wide range of beam movements and beam currents, which is very much required at the initial stages of operation and optimization in any SRS.

The quality of information that can be drawn from a pinhole array image is also affected by the horizontal and vertical separation between pinhole images and their relative contrast factors. Calculated intensity distributions of the x-rays on phosphor screen for 8 keV and 18 keV are shown in Figure T.3.4. A pinhole array with 1 mm pitch gives final image with more than five vertical points for the profile measurement even at high energies.
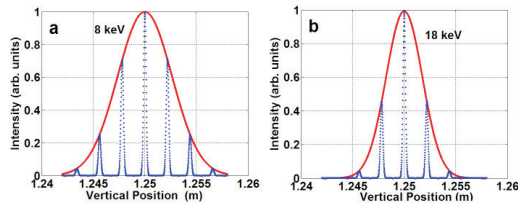
Fig. T.3.4: Calculated intensity distribution on the phosphor screen. Pinholes with 1 mm pitch and 20 µm diameter give good contrast factor for seven peaks at 8 keV (left), and five peaks at 18 keV (right).

2.3 Detector system

The beam profile is captured on the phosphor screen with a remote controlled zoom lens and a high resolution CCD camera. Zoom optics provides flexibility for imaging from high resolution mode (where only the central pinhole is visible), to the low resolution mode (where the whole pinhole matrix becomes visible). Schematic of the image detection system at BL-24 is shown in Figure T.3.5.
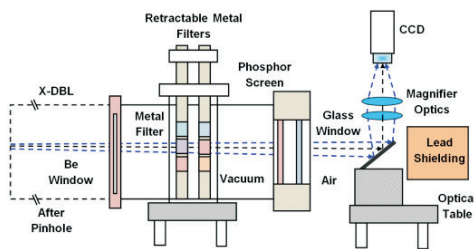
Fig. T.3.5: Schematic of the image detection system.

Image of beam spots on the phosphor screen is captured and processed to get beam size (σx, σy) and beam centroid in both the planes. Actual beam sizes are calculated by removing the total spread functions of the beamline from the measured values. Beam position stability is measured by tracking the centroid of pinhole image at the detector. Beam divergence is

measured by Gauss fitting of the intensity distribution of the peaks in a vertical column of beam spots. Beam emittance (ε) is determined by using measured beam size and known Twiss parameters of the source point by using

$$\sigma = \sqrt{\varepsilon\,\beta + (\eta\,\delta)^2} \tag{2}$$

where σ is the beam size, β is the beta function , η is the dispersion at the source point and δ is the energy spread. As β, η and other Twiss parameters of the source point are known from the calibrated models i.e. Accelerator Toolbox or LOCO, the emittance can be obtained from the measured beam sizes by using Eq.(2). Snapshot of the GUIs developed for online measurement of beam parameters at X-DBL [16] is shown in Figure T.3.6.
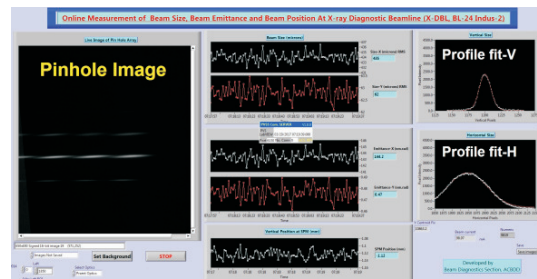
Fig. T.3.6: Snapshot of the GUIs used for online measurement of beam parameters.

3. Visible diagnostics

Visible light is extracted from the wide SR spectrum by using water cooled metallic mirror i.e. primary mirror. This visible light is optically processed to measure beam parameters by using optical methods such as telescopic imaging, interferometer [17], and π-polarization [18]. The longitudinal information of the beam is also measured by using fast photo detectors.

3.1 Visible diagnostic beamline BL-23

In Indus-2, the SR power from the dipole magnet is ~20 W/mrad at a stored beam current of 200 mA, and majority of this power falls within the x-ray domain. This high power component is discarded and only visible portion is retained (at 5 m) for the visible diagnostics [8]. We are using an approach similar to the split mirror with only lower half segment. Thus we are avoiding the complications associated in maintaining co-planar alignment of the two halves and adverse heating problems. The primary mirror made of copper substrate (80 mm X 50 mm X 10 mm) with 25 µm gold coating is kept at 45° to the horizontal. Its total horizontal angular acceptance is ~ 5 mrad. It can be moved parallel to its surface by stepper motor arrangement, allowing the mirror position to be carefully optimized with respect to the central x-rays core. Optimum water cooling mechanism is also provided to avert heating

problems. The temperature of outgoing cooling water of primary mirror is continuously monitored and interlocked with WCS in FE. A temperature rise exceeding 45 °C signals the beamline to close WCS. The mirror remains typically parked about ~ 0.5 mrad away from the beam centreline during normal operations.
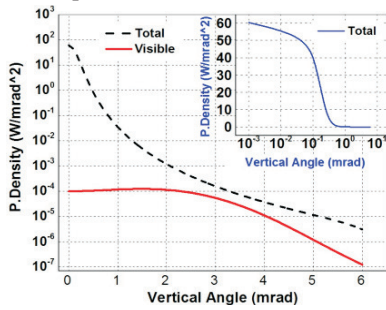
Fig. T.3.7: Angular distribution of the total power density and visible power density from a dipole magnet of Indus-2. Most of the SR power remains confined within 0.5 mrad vertical angle (inset).

The extracted visible light follows reflective and refractive optics, and is focused on the optical table in the dark room outside the shielding wall of Indus-2. Measuring detectors are kept at a distance of ~20 m from the source point in the dark room. Schematic layout of the V-DBL is shown in Figure T.3.8.
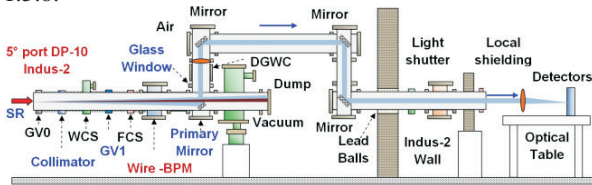
Fig. T.3.8: Schematic layout of the visible diagnostic beamline BL-23 in Indus-2

3.2 Angular acceptance of the beamline

The spatial resolution of profile measurement is limited by several factors such as diffraction error, curvature error and depth-of-focus error [19]. Curvature error is the horizontal broadening of image due to curved trajectory of electron beam in the dipole magnet. Depth-of-field error is the broadening of image in both the planes due to imaging of a moving source. The contribution due to each factor and its dependence on angular acceptance is

$$\Delta_{Curv\_max.} = \frac{\rho\theta_H^2}{8} \qquad (3)$$

$$\Delta_{Dof\_max.} = \frac{\rho\theta_H(\theta_H + 2\psi_{SR})}{4} \qquad (4)$$

where ρ and θ_H are the bending radius and horizontal angular acceptance of beamline, $\psi_{SR} \approx 0.45\,(\lambda/\rho)^{1/3}$ is the natural

opening angle of SR. The SR is emitted in a narrow cone, and diffraction error limits the ultimate resolution of the imaging system. Hoffmann treated the SR diffraction quantitatively by using Fraunhofer diffraction, and the diffraction contribution for σ-mode is given by

$$\Delta_{Diff\_rms.} = 0.21\,(\lambda^2\rho)^{1/3} \qquad (5)$$

where ρ and λ are the bending radius and wavelength of light. Angular acceptance of the V-DBL is optimized to minimize the effect of these errors and maximize the light output for imaging. Results for angular optimisation are shown in Figure T.3.9. Even at optimised angular acceptance ~7 mrad (H), resolution is mainly dominated by diffraction. Although visible diagnostics has certain limitations in transverse measurements but, it is very convenient to use it for longitudinal measurements as a non-destructive diagnostics tool. Results of incident flux density on the primary mirror for different energies are also shown in the Figure T.3.9.
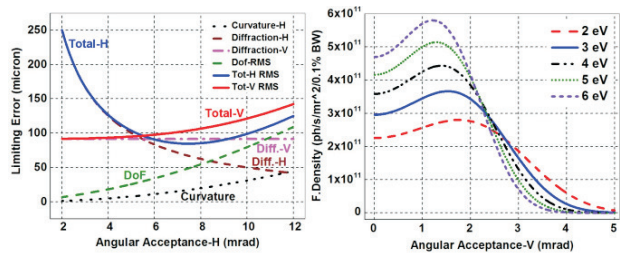
Fig. T.3.9: Calculated error contributions at different horizontal angular acceptance for visible diagnostics (left). Calculated incident flux density on the primary mirror at different energies (right).

After the primary mirror, the visible light is extracted out of vacuum through a high-quality Kodial glass window, and then reflected 90° by optical mirrors. A vertical offset of ~0.5 m between the two mirrors keeps radiation levels inside the adjacent optical hutch well within the safety margins even during beam injection. Visible light is focused at the image plane by a combination of achromatic doublet lenses of focal length 5350 mm.

3.3 Detectors

Instrumentation on the optical table includes beam profiler, dual sweep synchroscan streak camera (Model SC-10 Optronis) [20], avalanche photodiode, position sensitive detector and fast photo receiver. Streak camera is equipped with fast vertical synchroscan sweep unit and slow horizontal sweep unit to perform temporal measurements of the beam. Bunch train can be analyzed bunch-by-bunch with synchroscan sweep unit operating at half of Indus-2 RF frequency (505.812 MHz). Beamline is mainly used to measure the longitudinal beam parameters such as bunch length, bunch separation and bunch filling pattern.

4. Transverse measurements

4.1 Beam position

The variations in source position and emission angle cause flux loss or alignment problems at user beamlines. It becomes very critical for long beamlines operating at higher energies. Pinhole array is mostly used for the measurement of beam size and emittance, and its use for the measurement of source position and emission angle is less reported. Modified equations are used to find the exact correlation of source position and angle with position and intensity of various pinhole spots. Schematic of the vertical position of pinhole image at the phosphor screen from i^{th} pinhole is shown below in Figure T.3.10.
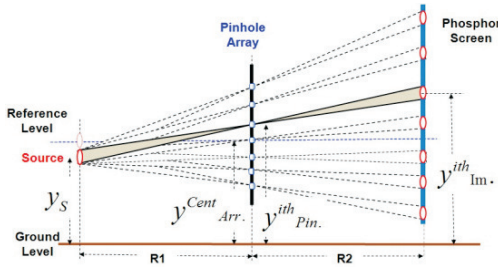
Fig. T.3.10: Schematic of the vertical position of pinhole image from i^{th} pinhole at the phosphor screen.

If there is only source position shift, at the image plane, whole pattern moves up/down in a direction opposite to the direction of movement of source point (y_s) but the maxima of the fitted gaussian remains at same position. Therefore the vertical position of image from y_{lm}^{ith} pinhole at phosphor screen (y_{lm}^{ith}) can be derived as [7]

$$y_{lm.}^{ith} = \left[\frac{R2 + R1}{R1}\right]\left(y_{Arr.}^{Cent.} + i^{th}\Delta\right) - \left[\frac{R2}{R1}\right]y_S \quad (6)$$

where $R1$ and $R2$ are the distances of pinhole array from the source and phosphor screen, respectively; y_s and $y_{Arr.}^{Cent.}$ are the vertical position of source point and pinhole array centre above the ground level respectively. Δ and n are the pitch and number of pinholes in a single column of the pinhole array. The variation in emission angle ($\Delta\phi_{V\_Angle}$) causes only shift in the position of Gaussian fitting of all the peaks, and the positions of individual peaks remain fixed. The maximum position of Gaussian is very sensitive to the angular changes and can be written as

$$y_{lm.}^{Peak\,Gauss\cdot} = \Delta\phi_{V\_Angle} \quad (R1 + R2) \quad (7)$$

Source position can be measured more precisely by averaging it over many pinholes as follows

$$y_S = \frac{1}{n}\sum_i \frac{R1}{R2}\left\{\frac{R2 + R1}{R1}\left(y_{Arr.}^{Cent.} + i^{th}\Delta\right) - y_{lm.}^{ith}\right\} \quad (8)$$

In X-DBL, SPM and pinhole array are designed in a single assembly unit, which can be moved remotely without any disturbance to the stored beam. Source position and emission angle can be measured by using equations discussed above. We could not make precise angular changes in the stored beam due to practical reasons, but positional changes were tested by moving SPM assembly. Pinhole array images were processed to measure the centroid of various pinhole spots captured on the phosphor screen for a known shift of the pinhole array assembly. For a total vertical shift of ± 125 μm from its mean position, measured results are closely matching (± 12 μm) with the theoretically calculated values obtained from pinhole images (Figure T.3.11) [7]. It was observed that SPM measurements start showing non-linear behaviour beyond a certain range.
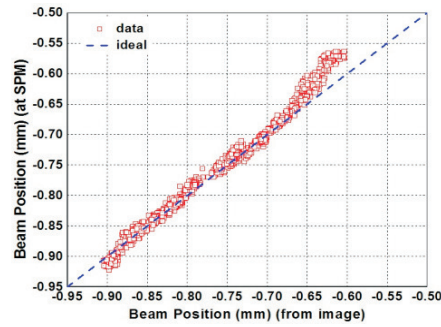
Fig. T.3.11: Comparison of the measured vertical position at SPM and pinholes.

4.2. Beam dispersion

One significant advantage of the x-ray pinhole camera over the UV/visible imaging is the stability of its final image, since the latter is susceptible to mirror vibrations in long transport line. This feature is used to measure dispersion function at the source point. Generally a set of beam profiles are taken with slightly different RF frequencies or different beam energies. From the measured displacements of the beam centroid, beam dispersion at the source point can be measured by using

$$\eta_{i=(x,y)}(s) = -\alpha_C \frac{\Delta_{i=(x,y)}(s)}{\Delta f_{RF}/f_{RF}} \quad (9)$$

where α_C is the momentum compaction factor, $\Delta_{i=(x,y)}$ is the measured change in beam centroid, and $\Delta f_{RF}/f_{RF}$ is the relative change in the RF frequency. The horizontal and vertical beam shift of ± 343 μm and ± 44 μm were measured at X-DBL during the RF frequency change of ± 5 kHz with respect to normal operating frequency of 505.8114 MHz as shown in Figure T.3.12. By using Eq. (9), measured horizontal and vertical dispersions at the X-DBL source point are found to be 0.253 m and 0.0325 m, respectively. Ideally vertical dispersion at source point is assumed to be zero, and this measured small dispersion is the spurious dispersion. Precise

value of vertical dispersion is very important to find exact beam sizes. Measured horizontal dispersion is also closely matching with the theoretically expected value at X-DBL source point [7].
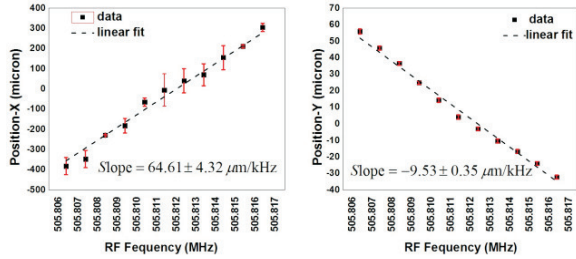
Fig. T.3.12: Measured data of the horizontal and vertical beam shifts along with their linear fit during RF frequency change of ± 5 kHz.

4.3 Beam size, beam divergence and beam emittance

The pinhole beam spots imaged on the phosphor screen are captured and image processed to get beam size and beam centroid in both horizontal and vertical planes.Typical graphs of measured horizontal and vertical beam sizes during the natural decay of beam current are shown in Figure T.3.13.
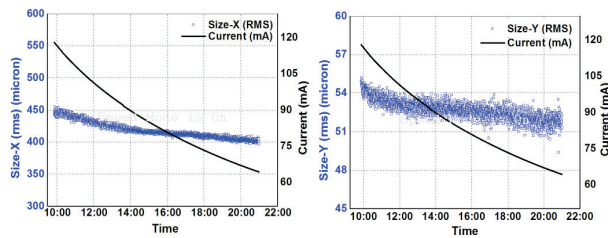
Fig. T.3.13: Typical graph of measured beam size horizontal (left) and vertical (right) during the natural decay of beam current from 118 mA to 64 mA.

Vertical beam divergence is measured from the intensity distribution of the pinhole spots in a column of the pinhole array. Online measured horizontal and vertical emittance at 1 Hz during the natural decay of beam current in Indus-2 are shown in Figure T.3.14.
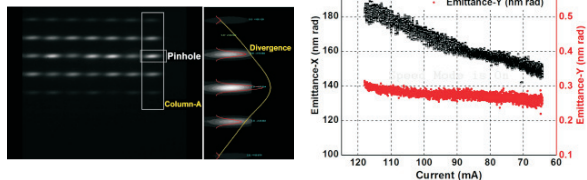
Fig. T.3.14: Photograph of the pinhole array image captured on the P-43 screen and measured intensity profile across column-A.Online measured horizontal and vertical emittance at 1 Hz during the natural decay of beam current from 118 mA to 64 mA in Indus-2.

4.4 Low emittance trials

Trial experiments were performed to operate Indus-2 SRS in lower horizontal beam emittance of ~ 45 nm.rad at 100 mA and 2.5 GeV. It will be useful for all user beamlines especially those who require small spot sizes or higher brightness. These experiments were performed by beam physicists [21], and diagnostic beamlines were used for online measurement of the beam sizes. Typical images of the pinhole array before and after applying low emittance optics are shown in Figure T.3.15. In the horizontal plane, the electron beam size was reduced from 430 ±20 µm to 310 ± 20 µm which was in agreement with theoretical predictions. Vertical beam size was also reduced from 65 ± 7 µm to 48 ± 7 µm by coupling corrections. During this switchover, the parameters of the bunch-by-bunch feedback system were optimized to control beam instabilities in the vertical plane.
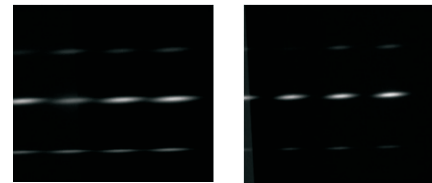
Fig. T.3.15: Typical images of the pinhole array before (left) and after (right) applying low emittance optics.

5. Longitudinal measurements

5.1 Bunch length and bunch separation

Bunch length, bunch separation and longitudinal dynamics studies of the charge particles are carried out by using streak camera system at V-DBL. It can provide temporal resolution down to few picoseconds for longitudinal measurements. Typical measured bunch length (RMS) and bunch separation of five consecutive electron bunches are 53±2.5 ps and 1.97±0.026 ns respectively as shown in Figure T.3.16.
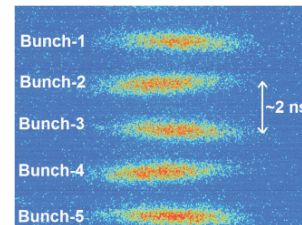
Fig. T.3.16: Typical bunch length measured using dual sweep synchroscan streak camera for five consecutive bunches at 75 mA beam current in Indus-2.

V-DBL was used to find longitudinal instabilities in the bunch train during commissioning of longitudinal multi bunch feedback (LMBF) system in Indus-2 by a designated team. Bunch centroid shift and bunch length of the bunch train were measured by using streak camera during LMBF optimisation.

Bunch centroid shifts were reduced from 35 ps to 10 ps RMS as shown in Figure T.3.17. It was observed that bunch length variations were also reduced.
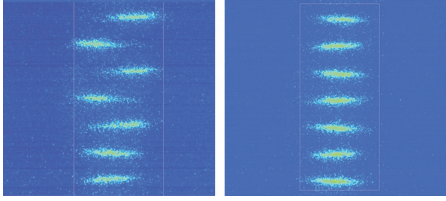
Fig. T.3.17: Typical images of the bunch train captured on streak camera with longitudinal multi bunch feedback OFF (left), and ON (right) in Indus-2.

5.2 Bunch filling level

Information regarding the number of filled bunch is called bunch filling pattern. This was measured by using APD and fast photo receiver at V-DBL. Snap shots of oscilloscope with bunch filling patterns of Indus-2 are shown below.
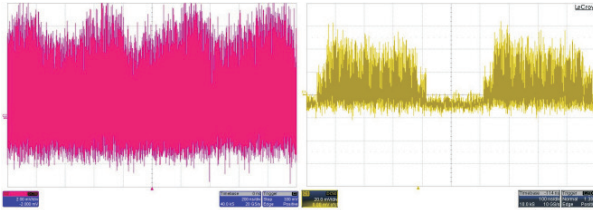
Fig. T.3.18: Snap shots of bunch filling patterns captured on oscilloscope, all 291 buckets filled (left), 200 filled buckets out of total 291 buckets (right).

5.3 Longitudinal impedance measurement

At low beam currents, the motion of a beam of charged particle is mainly guided by the magnetic lattice and RF cavities of the accelerator. The longitudinal distribution is determined by the equilibrium between radiation damping and quantum excitation. Natural bunch length σ_{zo} for a Gaussian distribution is

$$\sigma_{zo} = \frac{c\,\alpha_p}{2\pi\,f_{S0}}\,\sigma_{\varepsilon o} \qquad (10)$$

where α_p is the momentum compaction parameter, c is the speed of light, $\sigma_{\varepsilon o}$ is the relative energy spread of the beam and f_{so} is the synchrotron oscillation frequency. But at high beam currents, in addition to these interactions, the beam also interacts with its surrounding vacuum chamber through the electromagnetic fields generated by the beam itself. These fields can last for long enough to be experienced by a charge particle following the exciting charge, and it can perturb the energy or angle of the following particle's orbit. The dynamics of particle bunches due to their interaction with the environment (of the accelerator) through the beam-induced electromagnetic field is generally described in terms of *collective effects*. Collective instabilities usually limit the performance of an accelerator [1].

The electromagnetic interactions of the beam with its surroundings are described as wakefield in the time domain or impedance in the frequency domain. The impedance of an accelerator is usually considered to have three major contributions, (i) resistive wall, (ii) several narrow band resonators (modeling cavity-like objects), and (iii) one broad-band resonator (that models the rest of the ring). Both resistive wall and narrow band resonators are usually associated to slowly decaying wake fields, and produce *multi bunch effects*. The broad-band resonator mostly affects the particle dynamics within single bunch i.e. *single bunch effects* [22]. The maximum current that can be injected in an accelerator depends upon the impedance of the accelerator ring. The impedance of an accelerator ring is a complex quantity with real and imaginary parts. Real part is a resistance and manifests as an extraction of energy from the beam i.e. energy loss of the bunch. The imaginary part does not lead to any net energy loss within the bunch, but it causes energy transfer between the particles within a bunch. Ultimately it also causes bunch lengthening through increase in energy spread of the bunch. Therefore, these electromagnetic interactions can lead to deterioration of the quality of stored beam by parasitic energy loss of charge particles, or may make the beam unstable.

The major factors influencing the bunch lengthening are potential-well distortion (PWD) and microwave instability (MWI). PWD affects the equilibrium charge distribution of a bunch, and the deformed charge distribution inside the bunch can be obtained by solving the Haissinski equation [23]. Numerical and analytical solutions of the PWD equation are given for different longitudinal coupling impedances [24]. The impedance of storage ring is analyzed by applying these solutions/ impedance models on the measured bunch lengthening behaviour. These studies are performed by filling the charge in single bunch mode, where same charge acts as cause as well as probe.

In Indus-2, longitudinal profiles of electron bunch in single bunch mode were measured at injection energy 550 MeV and at final beam energy of 2.5 GeV [25]. The behaviour of measured bunch lengthening and phase advancing is analyzed by using dual sweep synchroscan streak camera. Typical image of the single bunch captured on streak camera is shown in Figure T.3.19. Measured bunch profiles for different beam currents upto 11 mA are shown in Figure T.3.19. In order to get precise information about the bunch centroid shift, bunch length change and asymmetry factor (bunch shape), the longitudinal distribution measured on

streak camera is fitted with asymmetric Gaussian function at each bunch current. Results of measured profiles are also shown in Figure T.3.19.
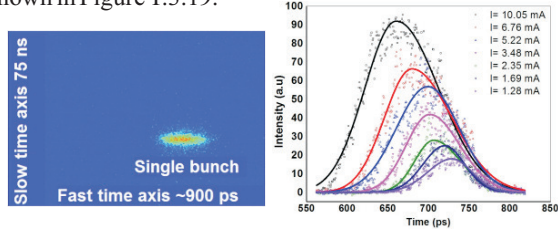
Fig. T.3.19: Snapshot of streak camera with single bunch filled in Indus-2 (left). Measured bunch profiles at different beam currents and their asymmetric Gauss fit (solid lines)

The effect of centroid shift and bunch lengthening is clearly observed with the increase of beam current. Numerical solutions [24] are compared with the measured longitudinal distribution at different beam currents. The estimated resistance contribution (R) of the vacuum structure using purely resistive impedance model is 1.350 ± 0.125 kΩ. Inductance value of the vacuum structure is estimated by comparing the measured bunch lengthening with the theoretical values of pure inductance model as shown in Figure T.3.20. The estimated inductive contribution (L) using purely inductive model is 180 ± 25 nH.
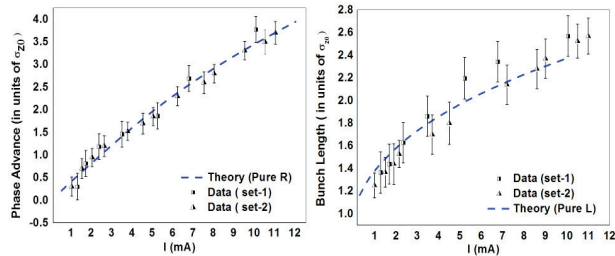
Fig. T.3.20: Comparison between the measured centroid shift and those calculated from a pure resistance model at different beam currents (left). Bunch length measured data and calculated values for a pure inductance case at different beam currents (right).

Above the microwave threshold, bunch lengthening occurs due to the combination of both PWD and MWI, and it follows the Chao-Gareyte scaling law [26] given by

$$\sigma_z \propto \left(\frac{\alpha\, I_{beam}}{v_S^2 E}\right)^{1/(2+a)} for\ I_{beam} > I_{Th} \quad (11)$$

where I_{beam} is the average beam current, v_S is the synchrotron tune, E is the beam energy and a is the scaling factor. In Indus-2, the threshold beam current for microwave instability at injection energy is expected to be $\ll 1$ mA per bunch. So all these measurements are taken above the

threshold value taken at injection energy. We got scaling equation σ_z (mm)$=6.67\ I(mA)^{1/3.66}$ by using Chao-Gareyte scaling law as shown in Figure T.3.21. The solid lines show the best fit of measured data set (taken at different times) for scaling parameter a in the range of 0.7 to 0.96. The combined vacuum chamber impedance estimated by fitting the measured data is $\sim 0.5\ \Omega$. After subtracting the contribution from the effective longitudinal coupling impedance derived from Zotter's formula [27], it gives a value for the longitudinal broadband impedance of $2.69\ \Omega$ [25].
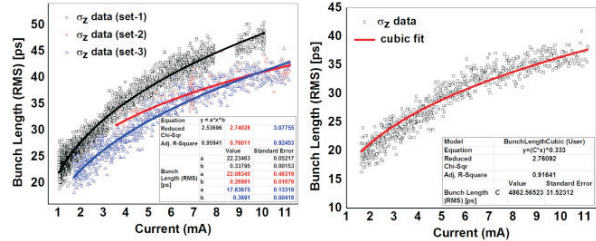
Fig. T.3.21: Measured data of bunch lengthening as a function of beam current and scaling law fit at injection energy (left). Bunch length data fitted with one-third dependence of beam current to get combined impedance (right).

6. Synchrotron radiation interferometer

Synchrotron radiation interferometer (SRI) is very useful for measurement of small beam sizes. The theoretical background of this method is described in the framework of wave-optics. It is based on Van Cittert-Zernike theorem which relates transverse source profile to its spatial coherence. The particle beam size is inferred from the measured fringe contrast [28, 29]. A double slit SRI was applied for the first time to measure small beam sizes at KEK-PF [30]. Advanced SRI with Herschelian reflective optics, intensity imbalance, and rotating pinhole designs have shown huge diagnostics potential of this technique. It is also implemented for the first time on a proton machine at LHC [31].

A quad slit SRI is optimized to measure the horizontal and vertical beam sizes at BL-23 in Indus-2 [32]. Schematic of the beam size measurement system is shown in Figure T.3.22. The intensity of the interferogram pattern [17] as a function of the position (y) is

$$I(y) = I_0 sinc^2\left(\frac{2\pi\, w_V}{\lambda R_2}y + \emptyset\right)\Big[1 \\ + |\gamma_y|\cos\left(\frac{2\pi\, d_V}{\lambda R_2}y + \psi\right)\Big] \quad (12)$$

where R_2, w_v and λ are the distance from the slit to detector, half aperture size of the vertical slit, and the wavelength of light respectively. d_v is the vertical slit separation. ψ and ϕ denote the phase and offset of the interferogram respectively. γ_y is the complex degree of spatial coherence. Visibility $|\gamma_y|$

can be derived by Fourier transform of the normalized source spatial distribution. For a Gaussian source it becomes

$$|\gamma_y| = e^{-2\left(\frac{\pi\, d_V\, \sigma_V}{\lambda R_1}\right)^2} \tag{13}$$

where R_1 is the distance of slit assembly from source and σ_v is the vertical beam size of SR source.
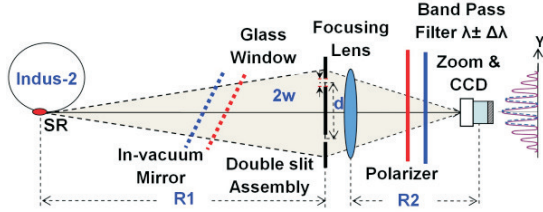
Fig. T.3.22: Schematic of SR interferometer for beam size measurement at BL-23 in Indus-2.

To optimize the SRI system, visibility curves are analyzed for a slit width of 2 mm, at 17 m from the source point. Visibility decreases with the increase of slit separation and beam size as shown in Figure T.3.23. Therefore the smaller the beam size, the higher can be the slit separation. Slit separation is also related to the error in beam size measurement through visibility.
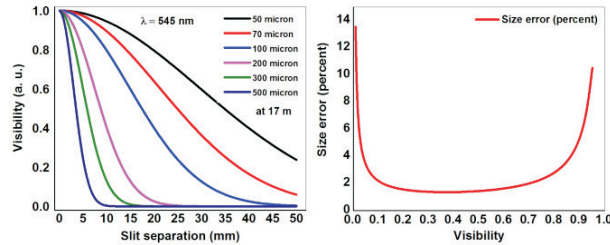
Fig. T.3.23: Theoretical visibility curves for various source sizes (left); variation of beam size measurement error w.r.t. visibility of interferogram (right).

For a detector which can detect minimum relative change in intensity dI/I_{AV}, there will be a relative measurement error in beamsize as

$$\frac{d\,\sigma_y}{\sigma_y} = \frac{\frac{dI}{I_{Av}}}{-2V\,ln(V)} \tag{14}$$

The error in beam size measurement at various visibilities of interferogram is also shown in the Figure T.3.23. It was found that relative size error increases at the extremes of visibility i.e. 0 and 1. For a reasonable value of detector sensitivity dI/I_{AV} ~0.5 %, it remains less than 2 % for a wide range of visibility. The error in measured beam size is almost constant in the visibility range of 0.2 to 0.6. SRI design is optimized to keep the visibility ~ 0.5 for a specified range of beam sizes. The system was simulated for visibility analysis of interferogram by using Synchrotron Radiation Workshop (SRW) code [33]. Typical images of the simulated interferogram for BL-23 are shown in Figure T.3.24.
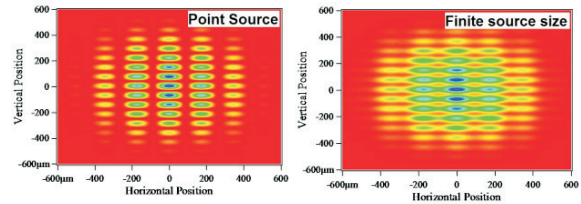
Fig. T.3.24: Typical images of simulated interferogram for a point source (left), and for finite source size (right) of Indus-2 beam.

SRI study will be used for measuring small beam sizes of few tens of microns during low emittance operations of Indus-2, and for the future high brightness SRSs in India. Even full reconstruction of the transverse beam shape is also possible by using rotating pinholes. This technique also provides the possibility of bunch resolved measurement with detector gating, which is very useful for studies related to injection dynamics, intra beam scattering and transverse instabilities.

7. Conclusion

Two diagnostic beamlines, viz. visible diagnostic beamline and x-ray diagnostic beamline have been successfully commissioned at dipole magnet DP-10 in Indus-2. Both of these beamlines are used regularly for online monitoring of beam parameters, and also for the dedicated beam physics experiments. Measurements performed on these beamlines have contributed significantly in the performance enhancement of Indus-2. Design study of synchrotron radiation interferometer will be useful for measuring small beam sizes in Indus-2. Studies related to injection dynamics, intra beam scattering and transverse instabilities are also possible with it.

8. Acknowledgement

References

[1] A.W. Chao, *Physics of collective beam instabilities in high energy accelerators*. New York: John Wiley & Sons Inc., 1993.

[2] M. Cornacchia, and H. Winick, SLAC-PUB-5164, 1990.

[3] M. Ferianis, "Optical Techniques in Beam Diagnostics," in *Proc. of 6th European Particle Accelerator Conf. (EPAC'98)*, Stockholm, Sweden, 1998, pp. 159-163.

[4] S. Takano, "Beam Diagnostics with Synchrotron Radiation in Light Sources," in *Proc. of IPAC'10*, Kyoto, Japan, 2010, pp. 2392-2396.

[5] I. Frank, and V. Ginzburg, "J. Phys. USSR," vol. 9, 1945, pp. 363.

[6] D. Rule, R.B. Fiorito, and W.D. Kimura, in *Proceedings of BIW '96*, Argonne, 1996.

[7] Akash Deep Garg, A.K. Karnewar, A. Ojha, B.B. Shrivastava, A.C. Holikatti, T.A. Puntambekar, and C.P. Navathe, *Nucl. Instrum. Methods Phys. Res. A*, vol. 754, 2014, pp. 15.

[8] http://www.rrcat.gov.in/technology/accel/srul/beamlines/visible_diag_beam.html

[9] H. Sakai, M. Fujisawa, K. Iida, I. Ito, H. Kudo, N. Nakamura, K. Shinoe, and T. Tanaka, *Phys. Rev. ST Accel. Beams*, vol. 10, 2007, pp. 042801.

[10] G. Kube, J. Gonschior, U. Hahn, P. Ilinski, G. Priebe, H. Schulte-Schrepping, Ch. Wiebers, S. Weisse, and C.G. Schroer, "PETRA III Diagnostics Beamline for Emittance Measurements," in *Proc. 1st Int. Particle Accelerator Conf. IPAC'10*, Kyoto, Japan, 2010, pp. 909-911.

[11] P. Kirkpatrick, and A.V. Baez, *Journal of the Optical Society of America*, vol. 38, 1948, pp.766.

[12] Cyrille Thomas, Guenther Rehm, Ian Martin, and Riccardo Bartolini, *Phys. Rev. ST Accel. Beams*, vol. 13, 2010, pp. 022805.

[13] V.K. Raghuvanshi, V.P. Dhamgaye, A.K. Sinha, and R.V. Nandedkar, in *International conference on synchrotron radiation instrumentation*, vol. 879 (1), Daegu, Republic of Korea, 2006.

[14] F. Sannibale, D. Baum, K. Holldack, N. Kelez, and T. Scarvie, "A Second Beam-Diagnostic Beamline for the Advanced Light Source," in *Proc. 20th Particle Accelerator Conf. (PAC'03)*, Portland, OR, USA, 2003, pp. 2527-2529.

[15] http://spectrax.org/php/download.php<code=spectra

[16] A. Ojha, Akash Deep, A.K. Karnewar, A.C. Holikatti, B.B. Shrivastava, T.A. Puntambekar and C.P. Navathe, "Development of LabVIEW based image processing algorithm for online measurement of beam parameters at x-ray diagnostic beamline of Indus-2", *Indian Particle Accelerator Conference, VECC, Kolkata, India* 2013.

[17] T. Mitsuhashi, "Spatial Coherency of the Synchrotron Radiation at the Visible Light Region and its Application for the Electron Beam Profile Measurement," in *Proc. of PAC'97*, vol. 1, Vancouver, B.C., Canada, 1997, pp. 766-768.

[18] A. Andersson, M. Boege, V. Schlott, A. Streun, and A. Ludeke, *Nucl. Instrum. Methods Phys. Res. A*, vol. 591, 2008, pp. 437.

[19] Weixing Cheng, "Synchrotron Light Monitor System for NSLS-II," in *Proc. 14th Beam Instrumentation Workshop (BIW'10)*, Santa Fe, NM, USA, 2010, pp. 478-482.

[20] http://www.optronis.com/de/home.html

[21] A.A. Fakhri, P. Kant, A.D. Ghodke, and G. Singh, *Rev. Sci. Instrum.*, vol. 86, 2015.

[22] G. Rumolo, and M. Munoz, "A study of collective single bunch phenomena in the ALBA ring," ALBA Project Document No. AAD-SR-BD-AN-0050 2005.

[23] J. Haissinski, *NuovoCimento*, vol.18, 1973, pp. 72.

[24] Joung-Moo Ko, Suk-Min Chung, Eun-San Kim, Chong-Do Park, and Takashi Naito, *Japanese Journal of Applied Physics 1A*, vol. 44, 2005, pp. 438.

[25] Akash Deep Garg, S. Yadav, M. Kumar, B.B. Shrivastava, A. Ojha, and T.A. Puntambekar, *Nucl. Instrum. Methods Phys. Res. A*, vol. 814, 2016, pp. 66.

[26] W. Chao, and J. Gareyte, *Particle Accelerators*, vol. 25, 1990, pp. 229.

[27] B. Zotter, CERN Report SPS/81-14, 1981.

[28] P.H. Van Cittert, *Physica*, vol. 1, 1934, pp. 2001.

[29] F. Zernike, *Physica*, vol. 5, 1938, pp. 785.

[30] T. Mitsuhashi, *Proc. of the Joint US–CERN–Japan–Russia School on Particle Accelerators*. Montreux and Geneva, Switzerland: World Scientific, 1998.

[31] G. Trad, E. Bravin, A. Goldblatt, S. Mazzoni, F. Roncarolo, and T.M. Mitsuhashi, "Beam Size Measurements Using Interferometry at LHC," in *in Proc. 5th Int. Beam Instrumentation Conf. (IBIC'16)*, Barcelona, Spain, pp. 583-588.

[32] Akash Deep Garg, M.H. Modi, and T.A. Puntambekar, *Nucl. Instrum. Methods Phys. Res. A*, vol. 902, 2018, pp. 164.

[33] O. Chubar and P. Elleaume, "Accurate and Efficient Computation of Synchrotron Radiation in the Near Field Region," in *Proceedings of the EPAC'98*, Stockholm, Sweden, 1998.